Hindawi
Geofluids
Volume 2023, Article ID 3399012, 22 pages
https://doi.org/10.1155/2023/3399012

Research Article

Mesoscopic Freeze-Thaw Damage Evolution Characteristics of Fractured Sandstone at Different Saturations

Yongjun Song, Yue Zhou, Huimin Yang, Chenjing Li, Jinghui Cao, Yinwei Sun, and Dongyang Han

College of Architecture and Civil Engineering, Xi'an University of Science and Technology, Xi'an, Shaanxi 710054, China

Correspondence should be addressed to Yue Zhou; 20204053032@stu.xust.edu.cn

Received 13 October 2022; Revised 13 December 2022; Accepted 15 December 2022; Published 20 April 2023

Academic Editor: Dongjiang Pan

To study the effect of saturation on the freeze-thaw damage of fractured rocks in cold regions, five prefabricated oval double-hole red sandstones with different saturations were prepared. Three-dimensional images of rock fractures were obtained by CT technology. The freeze-thaw damage mechanism and critical saturation of the red sandstone were explored through the fracture propagation evolution and quantitative characterization of the pore structure. The experimental results show that the pore size distribution can reflect the complex pore structure. Pores can be divided according to their sizes: small pores, mesopores, and macropores; mesopores account for the largest proportion and more than 70% of the total, and the proportion of mesopores in high-saturation sandstone (90% or 100%) increases under the action of freeze-thaw cycle. This is also accompanied by a small increase in the proportion of macropores. An 80% critical saturation of the sandstone was obtained. In addition, prefabricated cracks make the ice separation mechanism more likely to occur. The low-saturation sandstone mainly damaged the fracture area during freeze-thaw cycles, while the prefabricated cracks provided a good seepage channel for high-saturation sandstone. The corresponding rock bridge area eventually demonstrated a connectivity trend. This study more realistically reflects the freeze-thaw damage of actual rock masses in cold regions and provides a theoretical basis for the prediction of rock mass engineering disasters in cold regions.

1. Introduction

The occurrence of freeze-thaw cycles is one of the main factors affecting rock masses in cold regions [1]. After a rock mass experiences freeze-thaw cycles, the internal damage leads to a deterioration of its mechanical properties, which is a key engineering problem that must be solved in rock mass engineering construction and disaster prevention [2]. Freeze-thaw damage often occurs in many projects, such as roads, railways, tunnels, and building construction [3, 4]. Many scholars have studied the physical and mechanical properties of rock in a freeze-thaw environment, along with the freeze-thaw damage mechanism. Certain factors, such as the lithology (a combination of mineralogy and pore space that controls the durability to freeze-thaw cycles), freeze-thaw state, and stress conditions, affect the physical and mechanical properties of rocks [5], and common freeze-thaw damage mechanisms of rock include the volume expansion theory, hydrostatic pressure theory, segregation ice theory, and capillary and crystallization pressure theory [6]. However, considering that 9% volume expansion requires at least 91% saturation, rocks with incomplete saturation may not reach the threshold required for pore freeze-thaw cracking [7]. Further, incomplete saturation may also cause a decrease of engineering properties or damage of rock masses due to the accumulation of long-term freeze-thaw damage. The frost heaving force is affected by the fracture saturation of the rock mass. Al-Omari et al. [8] determined that the number of freeze-thaw cycles has a limited effect on frost damage, and the critical degree of water saturation is the main controlling factor for frost damage. However, it should bring the nuance that the impact of the number of freeze-thaw cycles (at least) can be significant. Therefore, analyzing the freeze-thaw damage mechanism of rocks with different saturations is of great significance to mitigate issues regarding frozen rocks in cold regions.

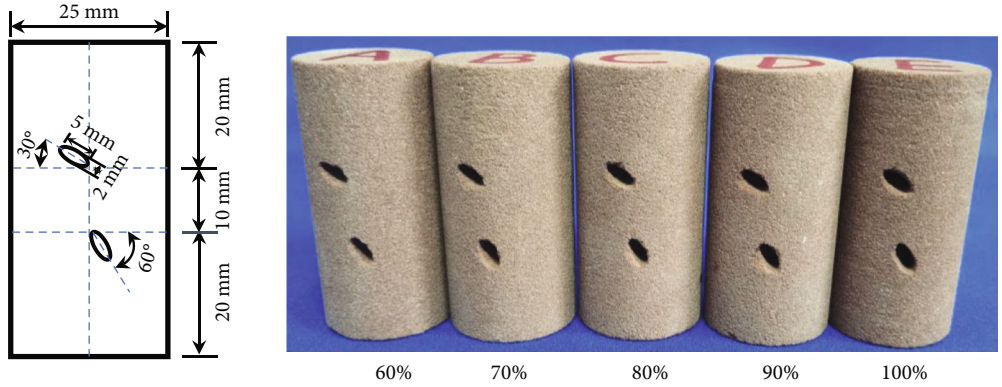

Figure 1: Geometry of the fracture space.

Several researchers have studied the freeze-thaw damage of rocks at different saturations. Huang et al. [9, 10] conducted acoustic emission tests on red sandstone at different saturations under freeze-thaw conditions, confirming the existence of a critical saturation and exploring its freeze-thaw damage mechanism; then, they found that the critical saturation that leads to a significant reduction of uniaxial compressive strength for sandstones under freeze-thaw is 60%~80%. Zhou et al. [11] analyzed the influence of water saturation on the fracture behaviour of rock materials by using the improved split Hopkinson pressure bar (SHPB) device; Chen et al. [12] studied the changes of the uniaxial compressive strength, wave velocity, and porosity, along with the appearance of welded tuffs with saturations varying from 0% to 95%; they found that the critical saturation is about 70%. Guha et al. [13] found that the mechanics and fracture toughness of saturated water sedimentary rocks generally declined with increases in the saturation. Liu et al. [7] used red sandstone to conduct indoor uniaxial compressive strength and p-wave velocity tests, finding that the freeze-thaw damage increased rapidly with increases in the freeze-thaw cycles when the saturation exceeded 60%. However, most of these studies have been conducted on the macro scale, and Deprez et al. [1] believed that some novel technologies should also be used to carry out mesoscopic research.

At present, scanning electron microscopy (SEM) [14, 15], nuclear magnetic resonance (NMR) imaging [16, 17], computed tomography (CT) [18], and other methods are primarily used to observe the generation, connection, and expansion of pores and microcracks in samples. SEM wears down the surface of the tested sample, and NMR has a poor microscopic characterization ability compared to CT. As a nondestructive testing method, CT technology can carry out the three-dimensional visualization characterization of the internal structure of rocks [19]. Park et al. [20] conducted freeze-thaw cycle tests on diorite, basalt, and tuff, and particle detachment, crack initiation, and propagation and porosity increase were detected using X-ray CT. Deprez et al. [21] studied the role of ink bottle pores in the freeze-thaw failure of olivine limestone; strain measurements showed that the critical saturation level was between 70% and 80%, and the CT technique was used to scan the freeze-thaw limestone samples at different saturations to explain the source of the critical saturation. Shields et al. [22] conducted CT scans on freeze-thaw mortar samples with saturations of 75%, 90%, 95%, and 100%, finding that the crack volume increased with increases in the saturation. Song et al. [23] used CT to scan sandstone samples with saturated intact, saturated fractured, and ice-filled fractured states during freezing and thawing to explore the evolution process of secondary fractures. However, most studies employing CT scans focus on freeze-thawed intact rocks with different saturations; however, since all the rocks contain defects such as cracks and joints, the fracture saturation affects the freeze-thaw damage of the rock.

Table 1: Rock sample numbers and basic parameters.

Sample number	Initial saturation (%)	Dry density (g/cm^3)	Porosity (%)	P-wave velocity (m/s)
A	60	2.175	12.67	2577
B	70	2.206	12.66	2688
C	80	2.231	12.65	2577
D	90	2.189	12.53	2525
E	100	2.211	12.50	2525

Cracks and joints, as weak structural planes of rock masses, greatly reduce their strength when subjected to freeze-thaw cycles [24, 25]. However, the geometry and location of prefabricated cracks affect the generation, expansion, and connection of microcracks in the process of freeze-thaw cycles of rock masses [26, 27]. Tian et al. [28] studied the fracturing behaviour of rock-like materials containing two V-shaped parallelogram flaws, which founded the crack failure modes depended largely on the dip angle of the V-shaped crack. Most existing studies are limited to the microscopic analysis of freezing-thawing intact rocks with different saturations or freezing-thawing fractured rocks. Ren [29] used CT to explore the mesoscopic damage mechanism of frozen fractured sandstone samples under uniaxial compression, and the results showed that the geometric characteristics of prefabricated cracks had an important influence on the dilation. Bai et al. [30] studied the failure modes of red sandstone samples containing two ice-filed fissures

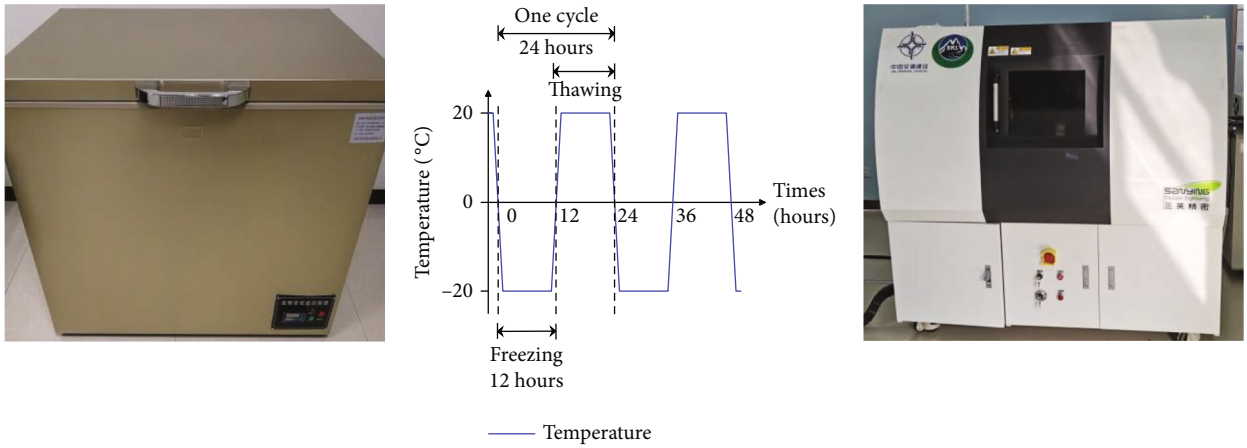

Figure 2: (a) DW-40 low-temperature test chamber. (b) Freeze-thaw cycle process. (c) Geotechnical multiscale high-resolution scanning analysis system.

under triaxial compression, which depend on the flaw combinations. However, at present, the study of the freeze-thaw damage of fractured rocks with different saturations by CT technology has rarely been reported, to the best of our knowledge. Therefore, the problems, such as (1) the freeze-thaw damage characteristics of rocks with elliptical fractures under the influence of different saturations, (2) the effect of elliptical fractures on the freeze-thaw damage of rocks with different saturations, (3) the extent of saturation of the naturally fractured rock mass, and (4) the extent of freeze-thaw damage to the rock by saturation, need to be addressed. Therefore, the CT technology is appropriate to study the mesoscopic changes of fractured rocks at different degrees of saturation due to freeze-thaw weathering. In this paper, fractured red sandstone with saturations of 60%, 70%, 80%, 90%, and 100% is used for freeze-thaw cycle tests. Through CT scanning technology, the secondary fracture evolution process of fractured sandstone is first studied, followed by the analysis of the mesodamage characteristics of the rock bridge area. Furthermore, this analysis of the critical saturation of red sandstone under different freeze-thaw cycles can rather provide useful data to predict the evolution of engineering properties of rock masses. The mesoparameters obtained are of great significance for understanding the damage characteristics of fractured rocks at different saturations in cold regions.

2. Materials and Methods

2.1. Preparation of Specimens. The test samples were selected from the near-homogeneous red sandstone of a mining area in the western cold regions of China. Because the CT scanning resolution is closely related to the sample size [31], 10 cylindrical samples—25 mm in diameter and 50 mm in height—were prepared according to the characteristics of the CT test system and the requisite specifications of most laboratory test rock samples. The oval flaws are also a common preflaws in practical engineering [32]. Therefore, this paper intends to use the drilling and cutting method to pre-

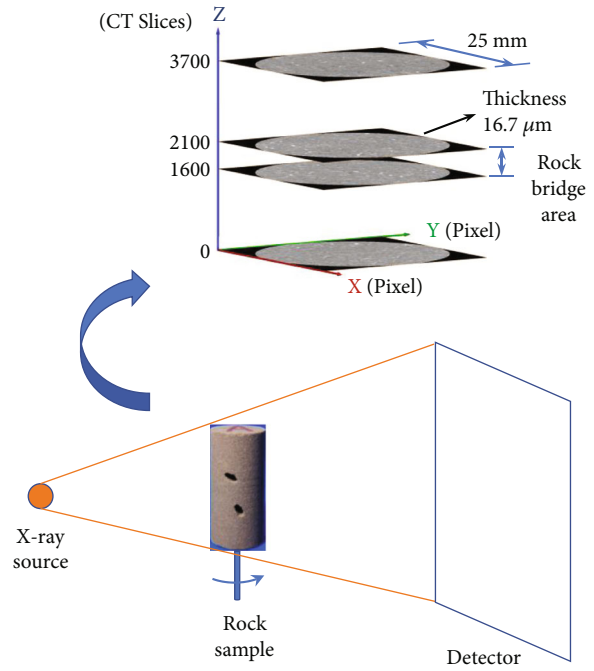

Figure 3: Sample placement and CT scanning principle.

fabricate elliptical fractures. In order to understand the effect of elliptical fractures on the freeze-thaw damage of rocks, the long axis of the crack was considered as 5 mm, the short axis 2 mm, and the rock bridge 10 mm. Five homogeneous rock samples were selected according to their longitudinal wave velocity and dry density. Because damage is prone to occur in the rock mass with the joint angles of 30°and 60° [33], we selected fracture inclination angles of 30°-60° (Figure 1). The rock sample numbers and basic parameters are listed in Table 1.

The rock samples were dried in an oven at 105°C for 48 hours; the longitudinal wave velocity and dry density were then measured after cooling, followed by saturation with a vacuum saturation device. When the vacuum reached

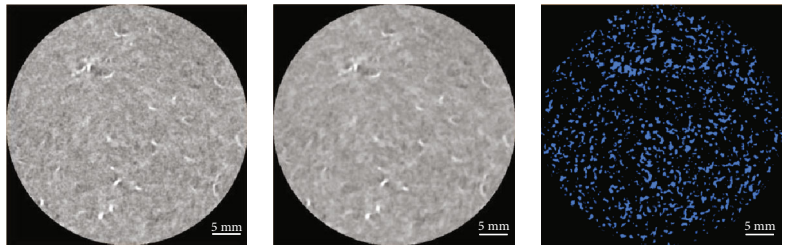

Figure 4: Images of specimen A after 60 F-T cycles. (a) Original image. (b) Filtered image (c) Optimized binary image.

-0.1 MPa, the rock samples were maintained for 24 hours to ensure complete water saturation. Subsequently, the quality control method involved placing the rock sample in a thermostatic chamber to make the water uniformly volatilize until the rock sample reached the necessary saturation, which was set to either 60%, 70%, 80%, 90%, or 100%. The setting method was described by Che et al. [34]. The formula is as follows:

$$m_t = m_d(1 - s_w) + s_w m_s, \quad (1)$$

where m_t is the quality of rock sample with corresponding saturation, m_d is the mass of rock sample after drying, s_w is rock sample saturation, and m_s is the completely saturated mass of rock sample.

As reported by Deprez et al. [21], to prevent water evaporation and maintain a uniform temperature distribution in the rock samples, the samples of different saturations were first sealed with aluminium foil and then wrapped in plastic tape.

2.2. Experimental Design and Principle

2.2.1. Freeze-Thaw Cycle Test. The number of freeze-thaw cycles was set to 0, 30, and 60. The process of one freeze-thaw cycle was to freeze at -20°C for 12 hours (according to the standard for test methods of engineering rock mass (GB/T 50266-2013)), followed by placing the sample at 20°C for thawing at room temperature for 12 hours [23]. The freeze-thaw box and freeze-thaw cycle process are shown in Figures 2(a) and 2(b), respectively.

2.2.2. CT Scanning. Using the geotechnical multiscale high-resolution scanning analysis system, CT scanning tests were carried out on five red sandstones with different saturations thawed after freezing and thawing 0, 30, and 60 times. The results of these tests were obtained as 16-bit images of 1900×1900 pixels and 3D images of fractured rock. Each rock sample was scanned three times, and 3700 sections were obtained per scan. The equipment parameters included a current of 190 mA, voltage of 150 kV, exposure time of 0.27 s, and spatial resolution of 16.7 μm. The sample placement and scanning principle are shown in Figure 3.

2.3. Image Denoising and Segmentation. Because various types of noise lead to CT image degradation (which affects the quantitative analysis of subsequent fracture extraction),

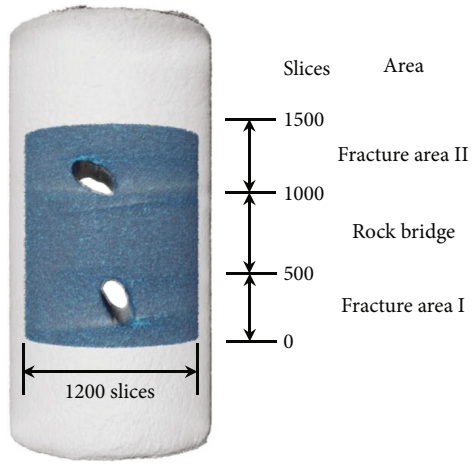

Figure 5: Extraction of regions of interest in rock sample and three areas.

the images are denoised first. The denoising methods include Gaussian filtering, median filtering, anisotropic diffusion filtering, and nonlocal mean filtering. In this paper, the median filter algorithm was selected to remove salt-and-pepper noise. This method includes a nonlinear digital filter that maintains the edge of the image [31]. The original image is shown in Figure 4(a), and the filtered image is shown in Figure 4(b). The red sandstone is basically composed of three components: pores/fractures, the matrix, and mineral inclusions. The grey value of pixels in the CT images is usually the average reflection of the density of all substances in rocks under certain scanning conditions [35]. The grey values of various substances in rocks are in the following order: minerals>matrix>pores/fractures.

To avoid boundary effect at the edge of the rock sample, the original 3D image was cropped and the same spatial position of the rock samples with different freeze-thaw conditions and different saturations were cropped based on the "Register Images" command. To further eliminate the boundary effect of the outer edge of the elliptical hole, a combined method of erosion and mask command was adopted. Two-dimensional image segmentation can divide the pixels of grey images into two categories, which are used to identify and quantify the pores and matrix in sandstone. At present, many methods have been proposed, including watershed threshold segmentation, interactive threshold segmentation, region-based segmentation, and deep learning-

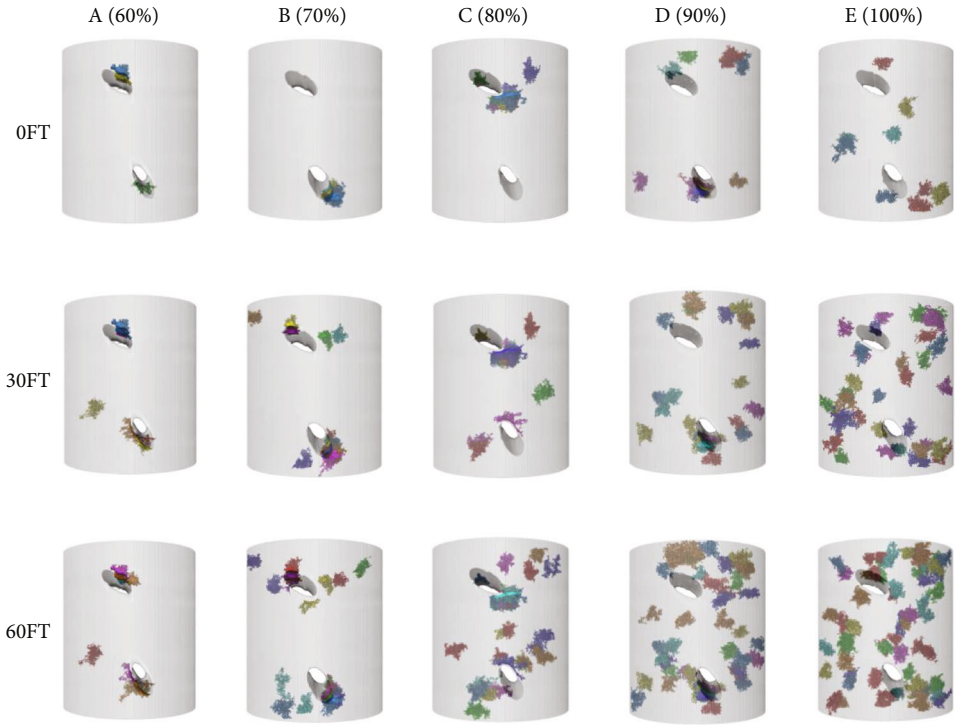

Figure 6: Fracture evolution process of five sandstone samples with different saturation.

based segmentation; however, different thresholds may lead to differences in the pore geometry and topological parameters [36, 37]. In this paper, interactive threshold segmentation and the "Interactive Top-Hat" algorithm were used to segment the image. Because the grey histogram of sandstone samples is unimodal, the segmentation threshold cannot be obtained directly according to changes in grey level. Therefore, the segmentation threshold of the CT images can be back-deduced according to the porosity measured by the rock sample at different saturations under corresponding freeze-thaw cycles [35]. The binary image after threshold segmentation is shown in Figure 4(c).

3. Experimental Results and Analysis

3.1. Three-Dimensional Reconstruction of Fracture Spatial Distribution. To understand the influence of prefabricated fractures on the evolution of pores and fissures in sandstone, a φ 21.71 mm × 25.05 mm core was selected as the research object (Figure 5). In order to reveal the evolution law of fractures in sandstone after freeze-thaw cycles, we omit the original connected pore structure and only show the parts with a volume > 0.5 mm^3. The fracture evolution process is shown in Figure 6. The fracture volume and fracture volume growth rate of each rock sample are presented in Tables 2 and 3. The fracture volume growth rate is the ratio of the crack volume increment before and after freeze-thawing to the fracture volume before freeze-thawing.

As shown in Figure 6, the spots and colours represent the size and location of the crack. The degree of fracture expansion of sandstone samples with different saturation levels is different even with the increase in the number of freeze-thaw cycles. The cracks near the fractures in samples might be produced by the drilling and cutting process when they were not frozen and thawed. Once the saturation was 60%, the fracture expanded around the elliptical hole and only a single fracture appeared in the rock bridge area. After 60 freeze-thaw cycles, the fracture propagation direction of the fracture I area demonstrated a trend of expansion along the short axis. Once the saturation was 70%, the fractures mainly appeared in areas I and II. The number of fractures in area II increased significantly, and the direction of expansion was around the ellipse. Finally, the expansion was at the edge of the rock sample. The direction of crack propagation

Table 2: The fracture volume values of five sandstone samples with different saturation.

FT	Fracture volume (mm^3)				
	A	B	C	D	E
0	11.7	17.0	22.8	23.4	23.2
30	12.9	19.4	27.9	30.0	31.8
60	15.2	24.7	37.8	40.5	52.2

Table 3: The fracture volume growth rate of five sandstone samples with different saturation.

State	Fracture volume growth rate (%)				
	A	B	C	D	E
$\Delta 1$[1]	10.3	14.1	22.4	28.2	37.1
$\Delta 2$[2]	29.9	45.3	65.8	73.1	125

[1]The change in parameters was obtained from 30 freeze-thaw cycles and 0 freeze-thaw cycles. [2]The change value of the parameters obtained from 60 freeze–thaw cycles and 0 freeze-thaw cycles.

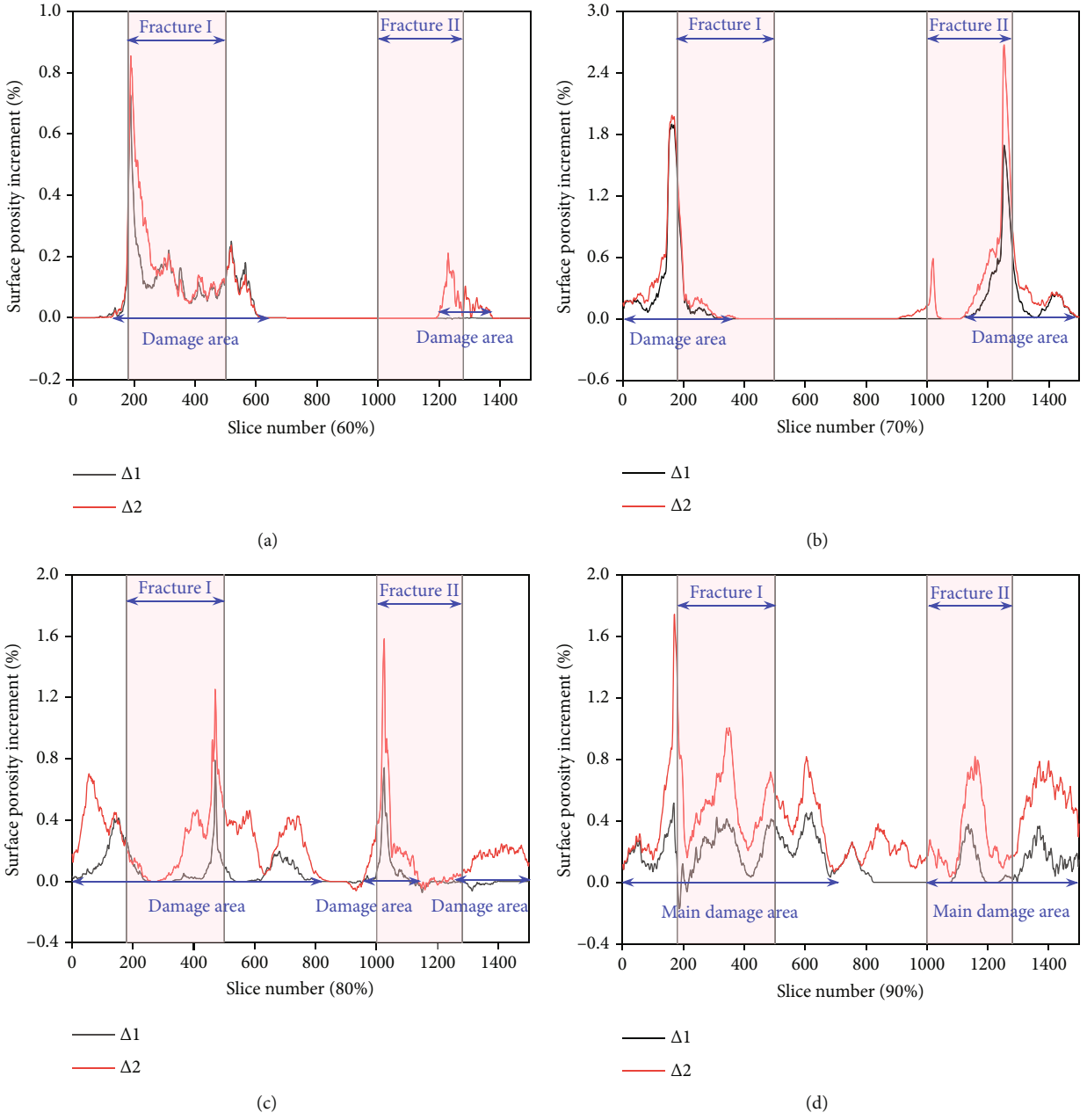

Figure 7: Continued.

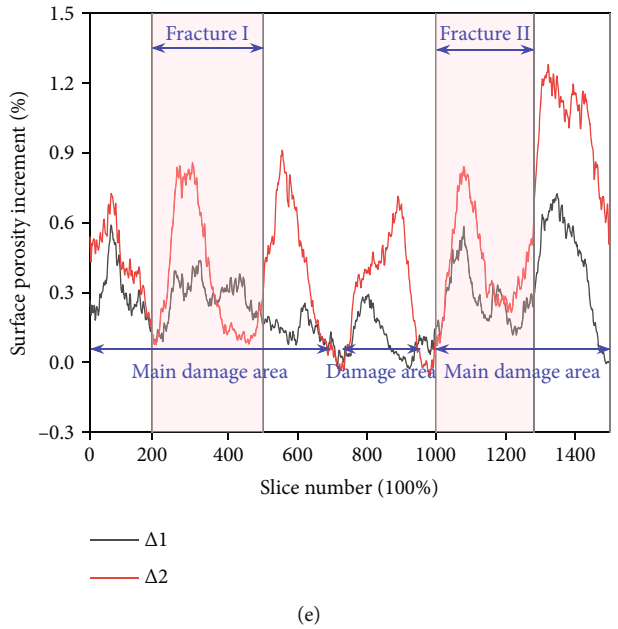

Figure 7: Variation curve of incremental value of surface porosity of rock samples with different saturations.

in fracture I area was similar to that under 60% saturation. After 60 freeze-thaw cycles of the rock sample with 80% saturation, an expansion trend was observed on the other side of the short axis of the ellipse in the rock bridge and the fracture II area. The expansion trend was similar to the fracture with rock sample saturation exceeding 80%. The fracture volume growth rate became larger, while the expansion trend was quite obvious. The fracture expansion of the fully saturated rock sample after 60 freeze-thaw cycles was critical among others. Compared to the initial unfreeze-thaw state, the fracture volume growth rate reached 125%. Because the water content is the highest and the freeze-thaw times are the largest in the completely saturated rock sample, the damage is the most serious. The volume growth rate of rock samples with 60% saturation was only 29.9% after 60 freeze-thaw cycles (Table 3).

In general, first, the fractures of the rock samples after freeze-thaw cycles expanded along the short axis of the ellipse, while appearing in fracture areas I and II. However, once the saturation exceeded 80%, the local damage caused by frost-heaving pressure gradually expands; the expansion positions of the fractures were gradually distributed in the rock bridge area, while being gradually connected. Finally, the fractures were distributed in almost the entire rock sample area.

To understand the change in porosity of each layer of the rock sample after the freeze-thaw cycle relative to the damage when it was not frozen and thawed, the three-dimensional fracture map of the selected rock sample was further analyzed and the porosity increment of each layer was calculated (Figure 7). The "$\Delta 1$" and "$\Delta 2$" in the figure represent the change in parameters obtained from 30 and 60 freeze-thaw cycles of the rock sample and zero times of freezing and thawing, respectively. This value greater than zero represents the damage area of the rock. As shown

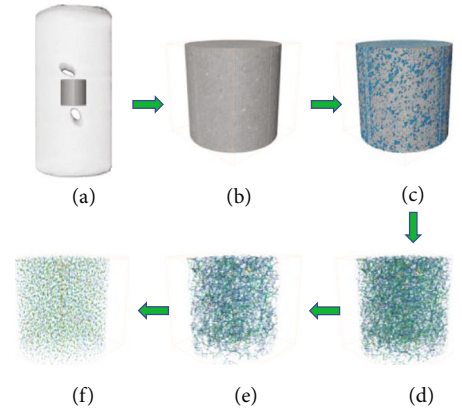

Figure 8: The workflow of extracting the pore network model. (a) Original volume. (b) The subvolume. (c) The binary subvolume. (d) The entire PNM, including nodes and links. (e) The nodes of the PNM. (f) Links in the PNM.

in Figure 7, with the increase in the number of freeze-thaw cycles, the incremental value of the sandstone surface porosity increased. The greater the saturation of the sandstone, the more obvious the increase in areal porosity, which is prominent in the fully saturated rock. Almost all of the rock samples had a damaged area, which was consistent with the fracture evolution diagram as illustrated in Figure 6. Once the saturation reached 60% and 70%, the damaged area appeared near fractures I and II. There was no damage zone in the rock bridge. Once the saturation exceeded 80%, the damaged area extended to the rock bridge. The greater the saturation, the more damaged area appears in the rock bridge. Once the saturation reached 80% and 90%, the main damage area appeared near fractures I and II. Moreover, the damage in this area was comparatively serious.

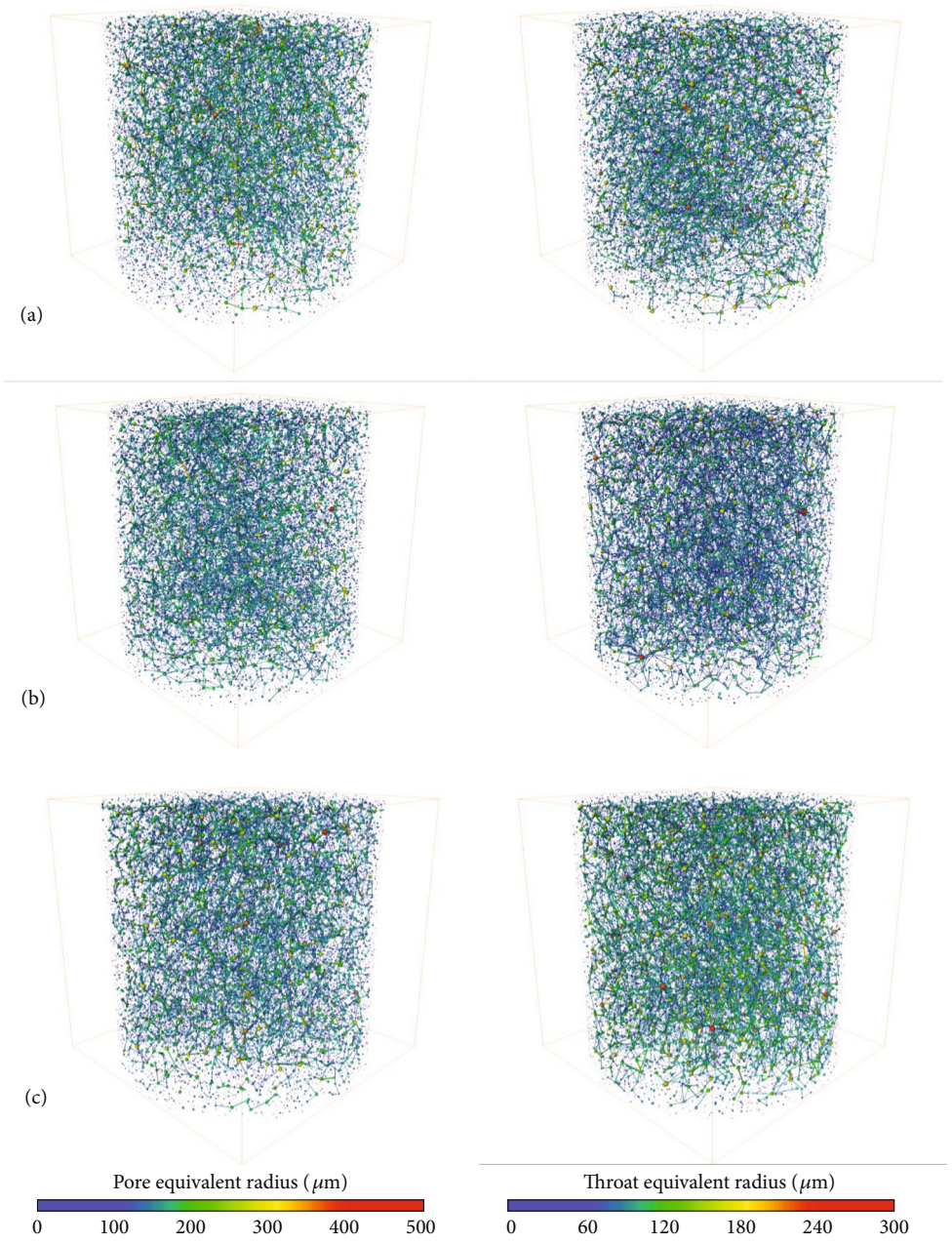

Figure 9: CT scan pore network model of three red sandstone samples with different saturations after 60 freeze-thaw cycles. (a) A (60%). (b) C (80%). (c) E (100%).

Once the saturation was lower than 80%, the damage areas mainly occurred in fracture areas I and II. Once the water content of the rock was low, the freeze-thaw cycle failed to damage the entire rock sample. Under the influence of prefabricated fractures, the damaged area extended from the fracture area to the rock bridge area once the saturation exceeded 80%. It demonstrated that for the rock with high water content, prefabricated fractures can provide channels for water seepage and accelerate the freeze-thaw damage of rock samples. Therefore, the critical saturation of this rock sample was preliminarily determined to be 80%.

As shown in Figure 7, after 60 freeze-thaw cycles, the rock bridge area of the low-saturation rock sample demonstrated no damage evolution features of microcracks. Therefore, the φ 8.35 mm × 8.35 mm core in the rock bridge was selected as the research object under Sections 3.2 and 3.3. The variation law of mesoscopic parameters corresponding to certain pores and fractures in the sandstone rock bridge was further analyzed.

3.2. Analysis of Pore Network Model Parameters

3.2.1. Quantitative Characterization of Pore and Throat Parameters. The three-dimensional pore network model (PNM) was extracted from the red sandstone samples with different saturations after 60 freeze-thaw cycles; the

Table 4: Pore and throat parameters.

Sample number	Freeze-thaw times	Pore			Throat		
		Average equivalent radius (μm)	Maximum equivalent radius (μm)	Number of pores	Maximum equivalent radius (μm)	Maximum length of the throat (μm)	Number of throats
A	0	39.66	302.56	38925	116.75	1428.94	6150
	30	39.73	290.46	39436	122.26	1388.36	6280
	60	39.84	283.38	40100	143.14	1317.15	6477
B	0	39.71	270.80	39640	112.84	1480.90	6197
	30	39.23	275.19	40445	120.42	1446.64	6488
	60	38.73	280.69	41500	146.65	1385.61	6796
C	0	39.95	326.01	39792	122.92	1306.66	6371
	30	39.68	317.53	40088	138.78	1298.02	6859
	60	39.39	302.69	40475	183.92	1286.62	7467
D	0	38.01	292.92	43447	114.69	1603.53	5573
	30	38.49	284.66	41724	115.62	1596.67	6897
	60	40.00	271.80	39828	117.37	1586.37	8108
E	0	39.62	290.17	40207	138.50	1373.01	5820
	30	39.97	287.68	39287	130.90	1386.90	7434
	60	40.45	281.23	38325	122.40	1411.53	8528

workflow is shown in Figure 8. Due to a small difference of the PNM observed by the naked eye, Figure 9 only shows the PNM of samples A, C, and E. The model transforms the pore-fracture system into pore throats and equivalent spheres; the throat is the channel that connects equivalent spheres, and the spheres represent the pores, whose volumes are approximately equal to the pore volume of the corresponding position. In the early use of this model, Lindquist et al. [38] extracted the 3D structure of sandstone based on skeletonization using the medial axis transform. The PNM of the pore-fracture structure was extracted using the AVIZO software, and the corresponding pore and throat parameters were calculated as shown in Table 4.

It can be seen from the pore network model that, after the freeze-thaw cycle, the pore network model from sample A (60%) to sample E (100%) becomes increasingly dense, and the number of throats increases, which is also shown in Table 4. After 60 freeze-thaw cycles, the number of throats increased by 327, 599, 1096, 2535, and 2708, and the growth rates of the number of throats were 5.32%, 9.67%, 17.20%, 45.49%, and 46.53%, respectively. When the saturation was lower than 80%, the number of throats increased slowly; however, when the saturation exceeded 80%, the number of throats increased rapidly, and the growth rate was close to 50%. After 60 freeze-thaw cycles, the number of red spheres in samples E increased more than those in samples A and C, indicating that the number of larger equivalent pore radius becomes greater when the saturation exceeds 80%.

After 60 freeze-thaw cycles, the pore and throat parameters change regularly. This change in the pore throat parameters can reflect the change process of internal pores and microcracks. Finally, it is found that the pore equivalent radius of sample A exhibits no obvious change law. As far as the average pore equivalent radius is concerned, those for samples A, B, and C remain basically unchanged, while those for samples D and E increase. That is, the higher the saturation, the more obviously the average pore equivalent radius changes. The maximum pore equivalent radius of sample B increases, while those of samples C, D, and E decrease. The maximum throat radius increases at first and then decreases with increases in the saturation, while the maximum throat length exhibits the opposite trend, with the turning point of both saturations being 90%. Based on this, it is preliminarily judged that the critical saturation of the sandstone may be 80%–90%.

In conclusion, after 60 freeze-thaw cycles, the number of pores in rock samples with a saturation ≥ 90% decreases while the number of throats increases, and the pore size expansion leads to connections between adjacent pores to form throats. The maximum pore equivalent radius decreases, the maximum throat radius exhibits a decreasing trend, and the maximum throat length increases, indicating that when the saturation is high, the rock sample is under the action of higher frost-heaving pressure and pore water pressure, and the macropores at large distances can connect with each other to form microcracks. When the saturation is less than 80%, the number of pores and throats increases, the maximum pore equivalent radius fluctuates with increases in the saturation, and the maximum throat radius increases. It is indicating that when the saturation is low, the frost-heaving pressure in the rock sample is small and no enough water to enter other pores; the freeze-thaw cycles mainly lead to interpore throat radius expansion, producing more pores around the pores.

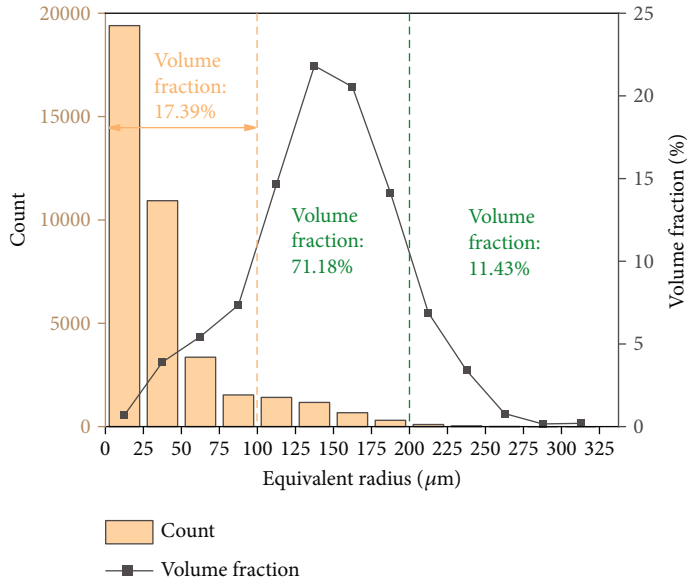

(a)

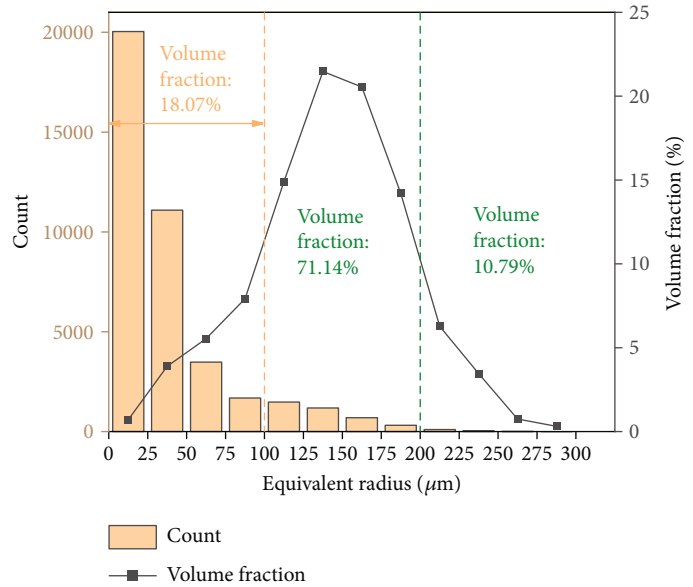

(b)

Figure 10: Continued.

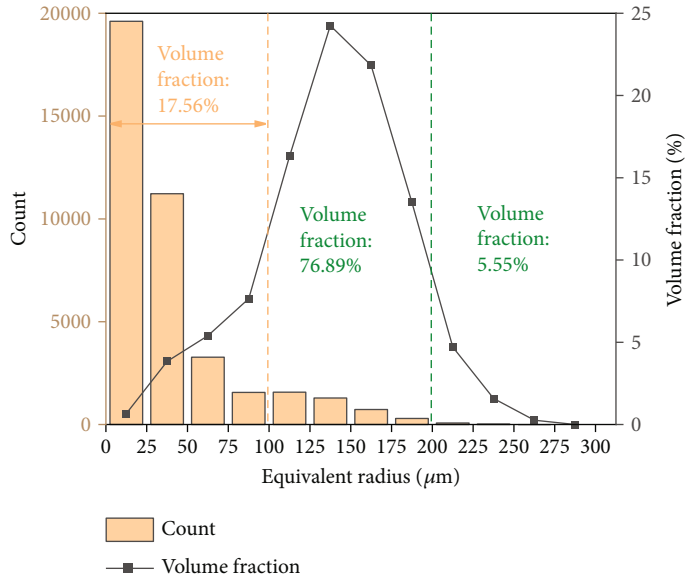

(c)

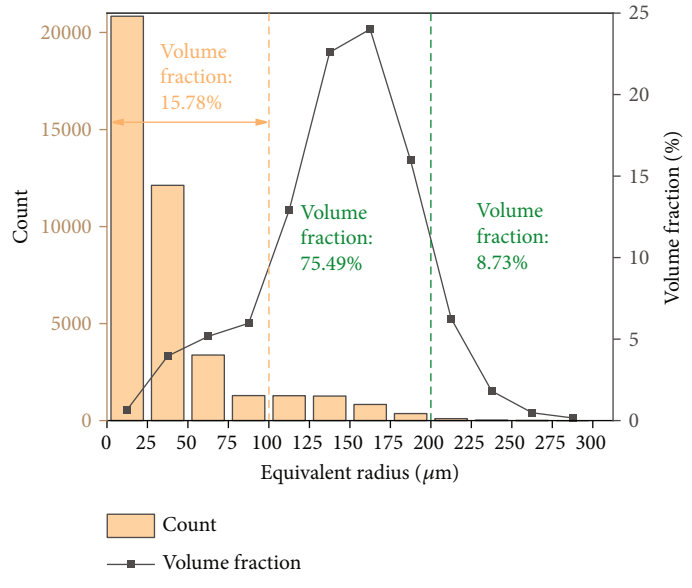

(d)

Figure 10: Continued.

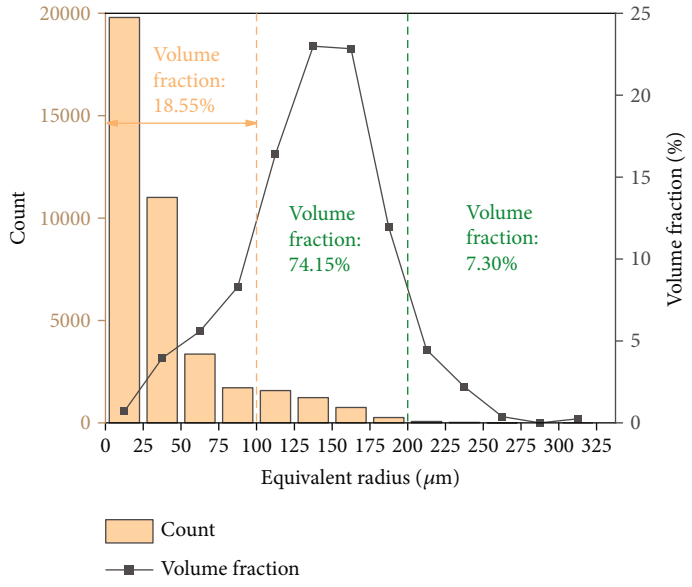

(e)

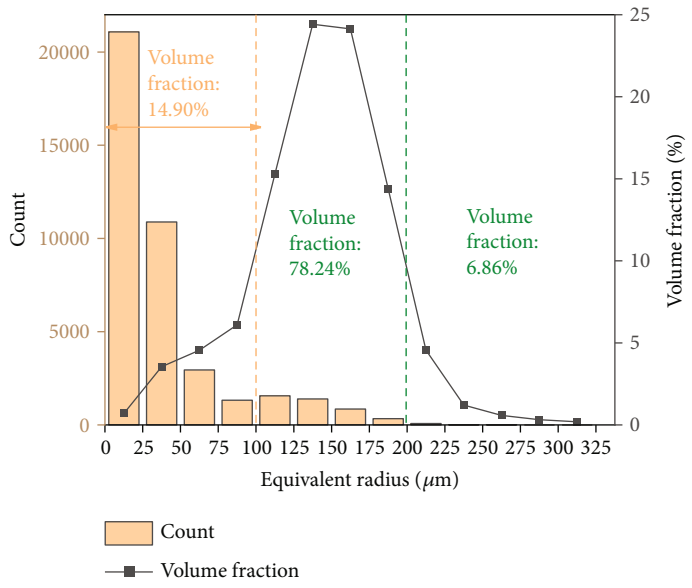

(f)

Figure 10: Continued.

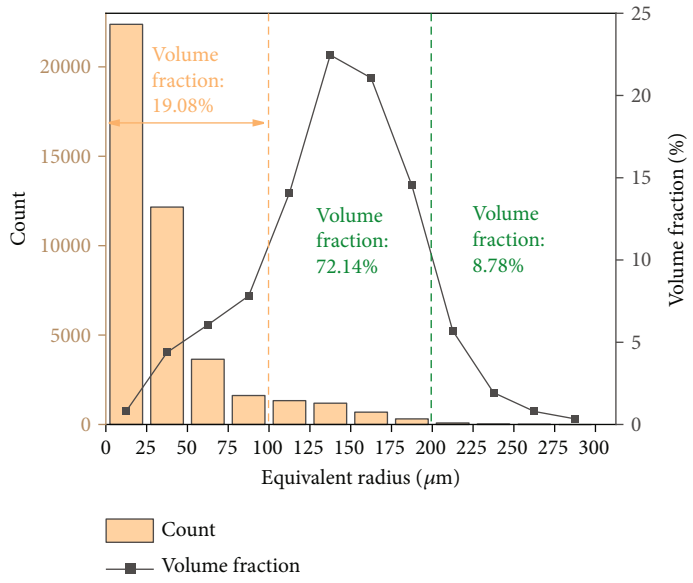

(g)

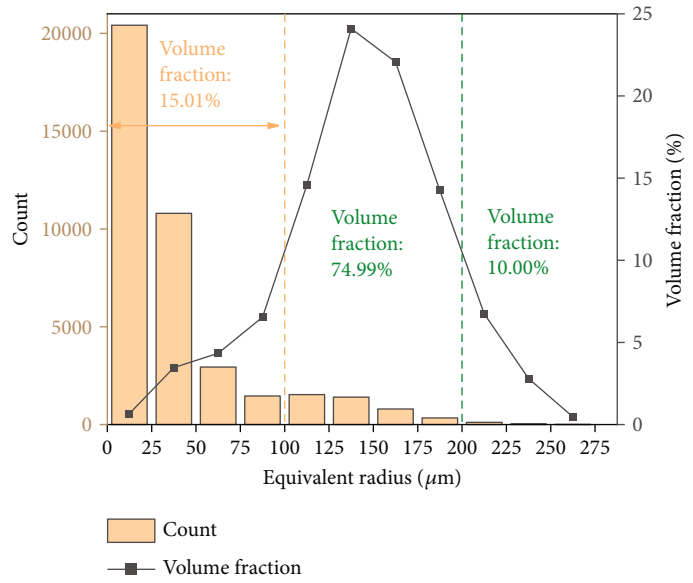

(h)

Figure 10: Continued.

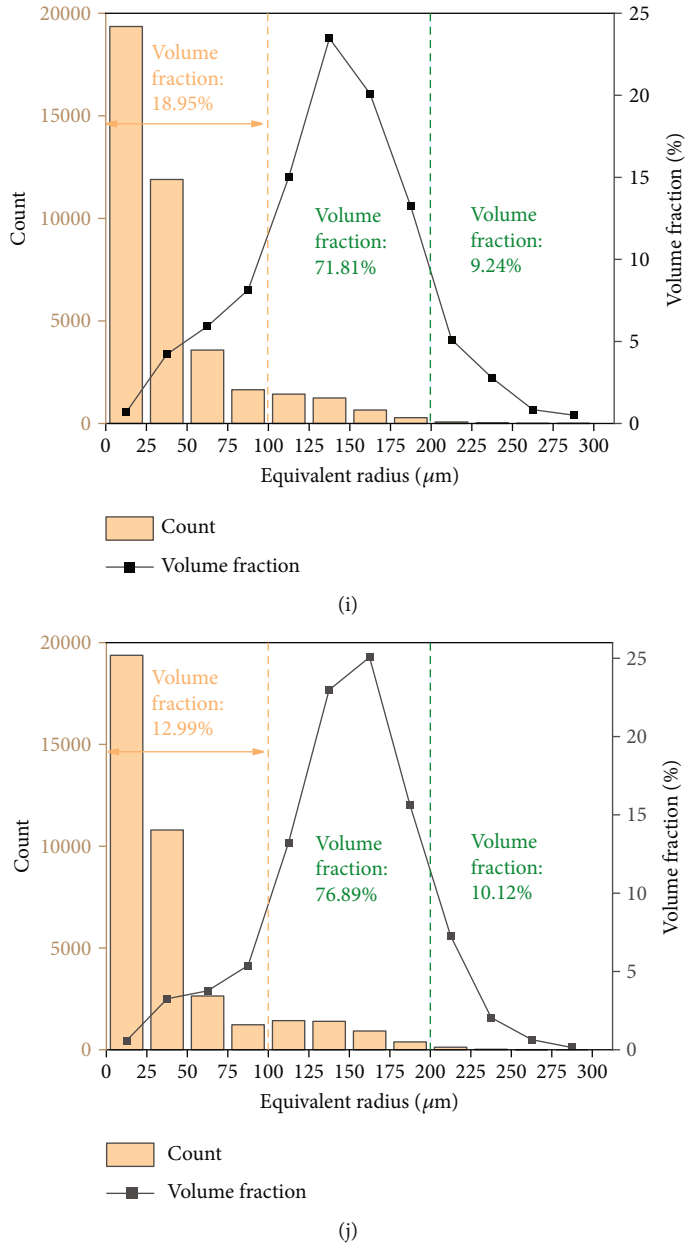

Figure 10: Distribution map of the equivalent pore radius and volume percentage of five red sandstone samples with different saturations after 60 freeze-thaw cycles. In (a, c, e, g, i), samples A, B, C, D, and E have undergone 0 freeze-thaw cycles, respectively. In (b, d, f, h, j), samples A, B, C, D, and E have undergone 60 freeze-thaw cycles, respectively.

3.2.2. Distribution of Pore Radius. However, the pore and throat parameters cannot completely and accurately describe the changes in the mesostructure, so the distribution of equivalent pore radius is described quantitatively. The pore size distribution can reflect the complex pore structure, and the pore size and volume ratio are shown in Figure 10. The pore size range of red sandstone with different saturations varies from 0 to 350 μm. According to this range, pore sizes lower than 100 μm, 100–200 μm, and greater than 200 μm are defined as small pores, mesopores, and macropores, respectively. The volume ratio of small pores is 10%–20%, that of mesopores is 70%–80%, and that of macropores is 5%–12%. It can be seen from Figure 10 that there are only a few macropores, and their proportion is the smallest. Although most pores are small pores, the volume ratio of mesopores is the largest, at over 70%.

In general, with increases in the equivalent pore radius, the number of pores first decreases significantly and then slowly; the pore volume ratio exhibits a "unimodal" distribution, which increases at first and then decreases. By analyzing the pore size distribution of red sandstone with different saturations before and after freeze-thaw cycling, it can be seen that the pore types whose pore proportion increases differ from sample to sample. The proportion of small pores in sample A increases by 0.68%, and the proportion of macropores in sample B increases by 3.18%; that is,

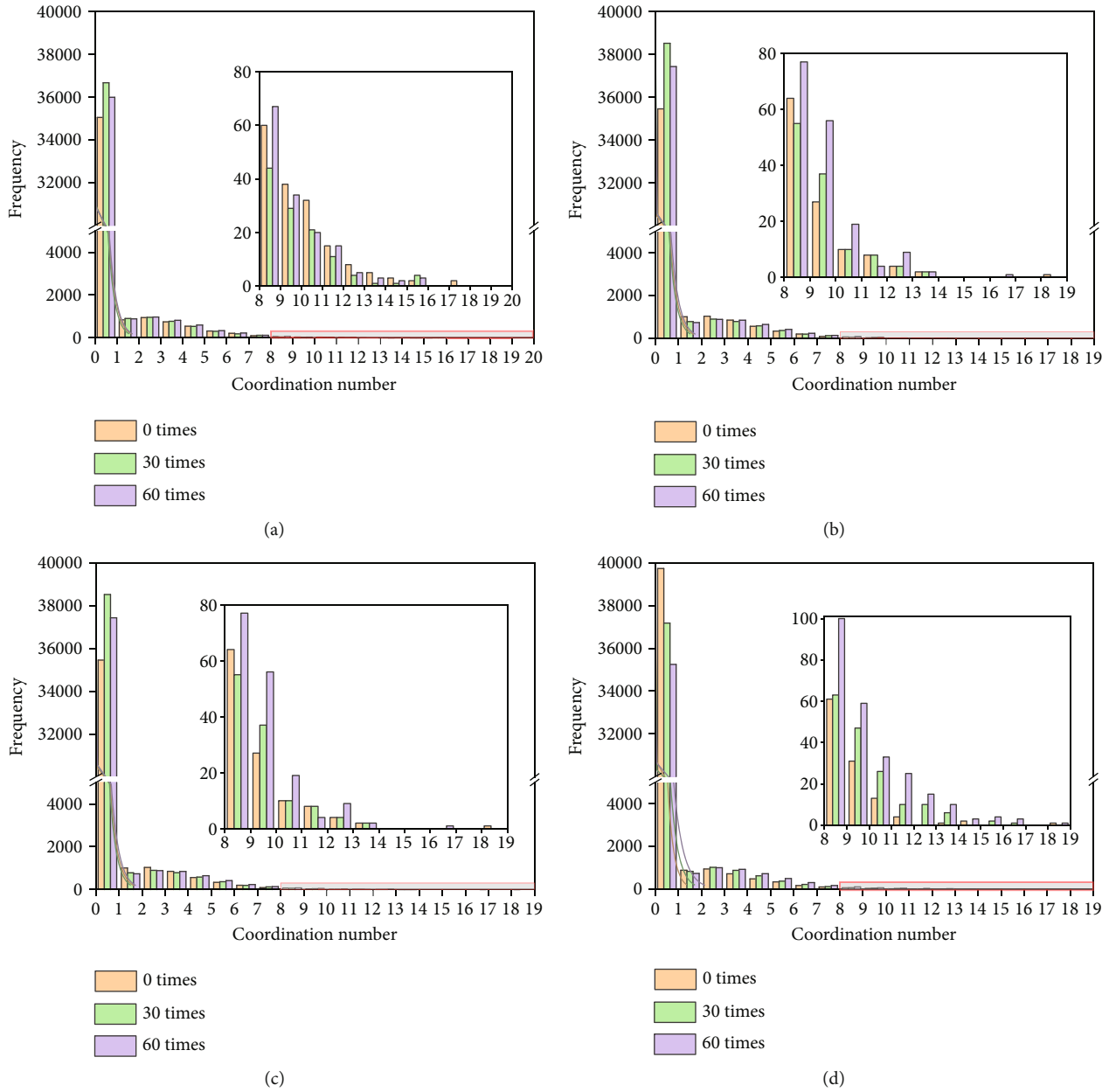

Figure 11: Continued.

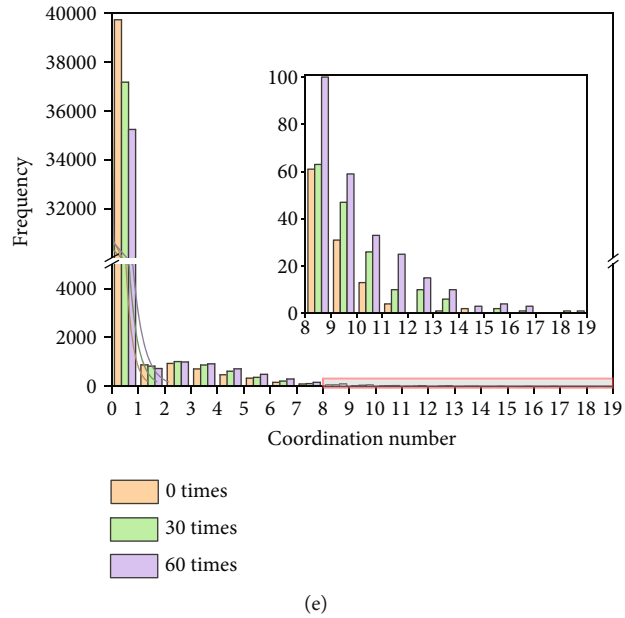

(e)

Figure 11: Histogram of the distribution frequency of the pore coordination numbers of five red sandstone samples with different saturations after 0, 30, and 60 freeze-thaw cycles. (a) A (60%). (b) B (70%). (c) C (80%) (d) (90%). (e) E (100%).

the type of pores with an increased proportion in rock samples with low saturations is uncertain. The proportions of mesopores in samples C, D, and E increase by 4.09%, 2.85%, and 5.08%, respectively, indicating that the proportion of mesopores increased significantly when the saturation was greater than 80%. Among them, the proportion of macro pores in sample D and E also increased, at 1.22% and 0.88%, respectively, indicating that when the saturation is greater than 90%, with increases in the number of freeze-thaw cycles, the proportion of macropores increases. However, since the volume ratio of mesopores is over 70%, mesopores play a major role in freeze-thaw cycles, and the proportion of mesopores increases obviously after the saturation exceeds 80%; therefore, the critical saturation may be 80%. At the same time, it is found that when the saturation exceeded 80%, the proportion of small pores decreases and the proportion of mesopores increases, which can be interpreted as the hydrostatic pressure mainly caused the generation of microcracks [23].

3.3. Pore Connectivity

3.3.1. Coordination Number. The coordination number is related to the connectivity of rock pores and reflects the spatial characteristics of the pore system. The number of throats connected to pores is defined as the pore coordination number; the larger the coordination number, the better the pore connectivity, the better the reservoir properties, and the greater the degree of internal damage after freezing and thawing. The frequency histogram of the coordination number distribution is shown in Figure 11. The distribution is exponential, ranging from 0 to 18, but mainly is 0. That is, most of the pores are isolated pores, a small proportion of the pores are connected to 1 to 6 throats, and very few pores are connected to more throats; therefore, the pore connectivity is poor. It can be seen from the curve of the exponential distribution that samples A, B, and C remain basically unchanged before and after freeze-thaw cycles and samples D and E move slowly to the right with increases in the freeze-thaw times, indicating that the pore coordination number increases gradually. It can also be seen from the local enlarged figure that, when the coordination number is 8, samples A, B, and C fluctuate with increases in the freeze-thaw times, while samples D and E increase in a step-wise manner. This further shows that the freeze-thaw cycle leads to the connection of pores inside the rock sample, and the damage of the rock sample is intensified. For high-saturation rock samples, during the thawing process, external water fills previously isolated pores and cracks, increasing the frost-heaving pressure. The freeze-thaw effect significantly destroys the connectivity of high-saturation rocks.

The average coordination number of the five saturation samples with increases in the freeze-thaw times was analyzed, as shown in Figure 12(a). The average coordination number of samples A and B increased slightly, followed by that of sample C; those for samples D and E increased the most. With the increase in the number of freeze-thaw cycles, the average coordination number of samples A, B, and C first decreases slightly and then increases. The average coordination number of samples D and E shows an approximate linear increase trend, and the correlation coefficient is above 0.97, indicating a high degree of fitting. And the slope gradually increases with increases in the saturation. After 60 freeze-thaw cycles, the average coordination number of samples with saturations less than 80% increases by about 0.01, and the average coordination number of samples with saturations more than 80% increases significantly, reaching 0.15, indicating that the pore connectivity is significantly enhanced.

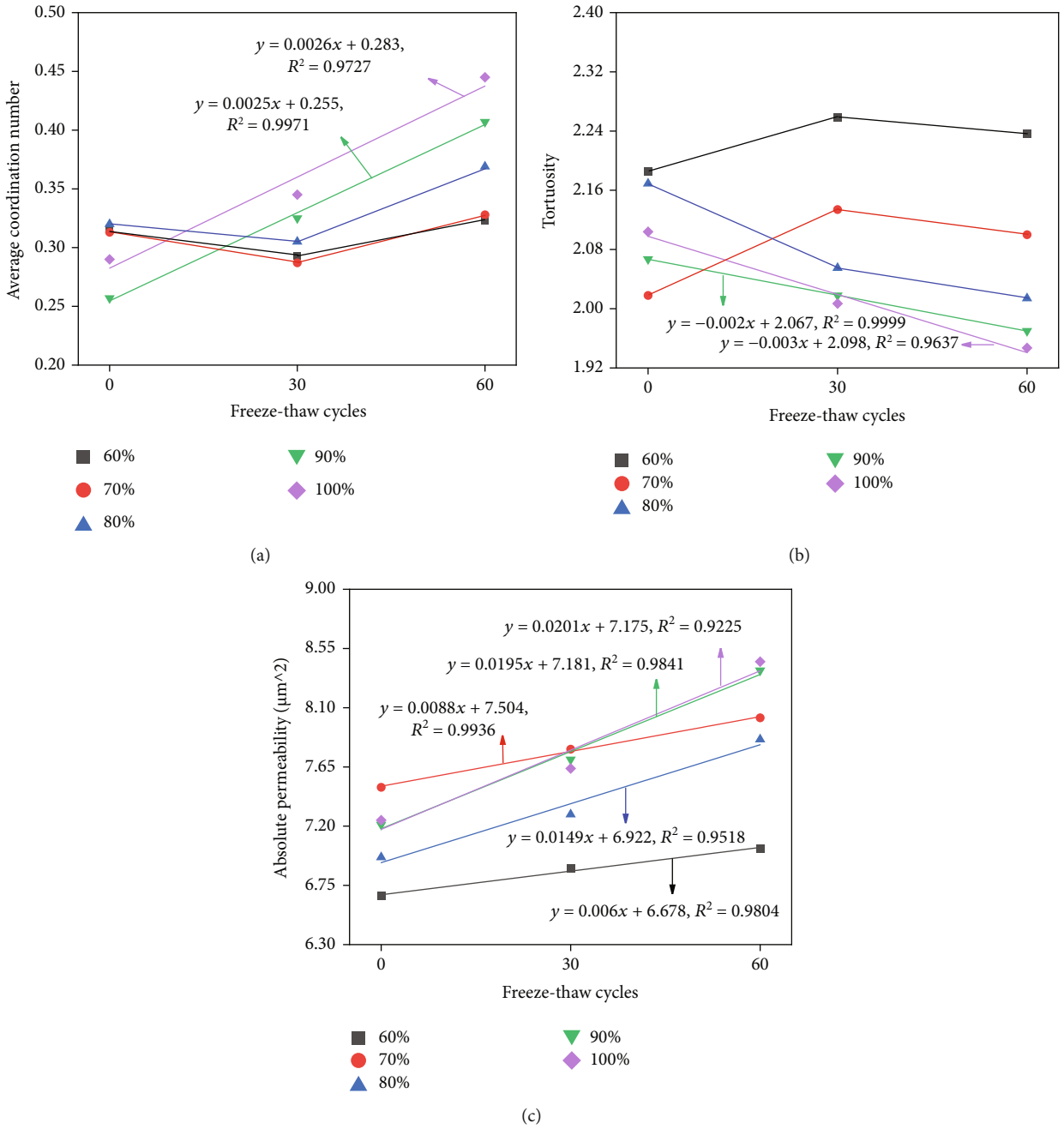

Figure 12: Connectivity curves of five red sandstone samples with different saturations after 0, 30, and 60 freeze-thaw cycles. (a) Average coordination number. (b) Tortuosity. (c) Absolute permeability.

3.3.2. Tortuosity. Tortuosity is an inherent property of porous rock [39]. When a fluid flows through a rock mass, it enters the tortuous channel, and the tortuosity represents the complexity of the fluid migration path in the rock. The smaller the tortuosity, the greater the damage degree of the rock after freeze-thaw cycles. Mathematically, tortuosity is defined as the ratio of the length of the tortuosity path to the longitudinal distance of the sample [40–43]:

$$\tau = \frac{L_e}{L}, \tag{2}$$

where τ is the tortuosity, L_e is the average length along the tortuous path, and L is the longitudinal distance of the fluid through the rock sample. In this paper, Avizo's centroid path tortuosity module is used to measure the tortuosity:

$$\tau = \frac{l}{H}, \tag{3}$$

$$l = \sum d(i). \tag{4}$$

This module is calculated by the centroid on each plane following the path formed by the binary image, where l is the

length of the path passing through the centre of mass in the z-axis direction and H is the number of planes in the z-axis direction; the value is taken as 500.

The tortuosity of the five saturation samples with increases in the freeze-thaw times was analyzed, as shown in Figure 12(a). With increases in the number of freeze-thaw cycles, the tortuosity of samples A and B first increases and then decreases. Within the error margin, the possible reason could be attributed to the low saturation of the rock sample, which extends the fractures laterally along the short axis of the ellipse. Moreover, the length of the seepage path and the tortuosity subsequently increases. When the freeze-thaw cycles are 60, the minimum length of the seepage path decreases, which makes the tortuosity decreases. With increases in the number of freeze-thaw cycles, the tortuosity of sample C decreases slowly, the tortuosity of samples D and E shows an approximate linear decrease trend, and the correlation coefficient is above 0.96, indicating a high degree of fitting. And with increases in the saturation, the degree of tortuosity decreases further. When the saturation exceeds 80%, the freeze-thaw cycle causes damage, the microcracks increase, the minimum length of the seepage path decreases, the sample connectivity increases, and the tortuosity decreases.

3.3.3. Absolute Permeability. The permeability can be calculated according to Darcy's law [44]. In this paper, the absolute permeability of the samples is calculated using the "Absolute Permeability Experiment Simulation" module in the Avizo software; subsequently, the absolute permeability of samples with five kinds of saturation is fitted with the increase in the freeze-thaw times. The fitting curve and correlation coefficient are shown in Figure 12(c), and the correlation coefficient is above 0.92. The curves of samples A, B, C, D, and E after fitting are all linear, and the fitting slopes are 0.006, 0.0088, 0.0149, 0.0195, and 0.0201, respectively. That is, the absolute permeability of the five kinds of saturation samples increases with increases in the freeze-thaw times. The absolute permeability of samples with saturations above 80% increases to a similar degree with a slope of 0.02, while those with saturations below 80% increase to a similar degree with a slope of 0.01. The fitting results show that the connectivity of samples with saturations more than 80% significantly deteriorate after freeze-thaw cycles. It must be mentioned that it is just to show the trend in Figure 12. It can hardly be generalized because only one sample was test for each condition. Despite all this, the observed trends are interesting and worth showing.

4. Discussion

In this study, first, the evolution characteristics of 3D fractures are analyzed. Subsequently, the variation law of mesoparameters of the pore network model along with the connectivity in the rock bridge area was discussed. It has been found that 80% may be the critical saturation of red sandstone samples, which is confirmed by the growth rate of the throat number, the maximum throat radius, the volume ratio of different pore types, the coordination number, the tortuosity, and the permeability changes. A similar critical saturation was found in a study by Deprez et al. [21]. Red sandstones with a low saturation (less than 80%) experience less damage, while highly saturated rocks are severely damaged after 60 freeze-thaw cycles.

4.1. Mesoscopic Freeze-Thaw Damage Mechanism under the Influence of Saturation. The freeze-thaw damage mechanism under the influence of saturation is shown in Figure 13. Saturation largely affects the degree of mesoscopic damage in freeze-thawed rocks. Some pores in low-saturation rocks contain water, and the pore volume expands during freezing. Because it is difficult for the frost heave force generated by the low water content to reach the critical tensile strength of the pores, the frost heave force is released after thawing, and there is not enough water to enter other pores, leading to lower freeze-thaw damage to the rock [45]. When low-saturation rock (<80%) is frozen, the content of ice increases, which can be used as a cementing material under the frost heaving force to provide adhesion and play the role of reinforcement; this strengthening effect is positively correlated with the initial saturation [46]. Despite experiencing 60 freeze-thaw cycles, the freeze-thaw effect of low-saturation rock samples is not obvious (Figure 6), which manifest in a small increase in the proportion of small pores and macropores, at 0.68% and 3.18%, respectively. The specific performance of the high-saturation rock samples is reflected in the obvious increase in the proportion of mesopores and macropores, and the volume of mesopores accounts for the largest proportion; therefore, mesopores play a dominant role in the freeze-thaw cycle. It should be noted that Ruedrich et al. [47] found that rocks with low saturation can also experience cumulative fatigue damage and collapse after up to 1400 freeze-thaw cycles.

The freeze-thaw damage mechanism of completely saturated rock follows volume expansion theory and hydrostatic pressure theory. The initial saturation is greater than 91%, and the pores satisfy the closed space, which provides appropriate conditions for the development of ice pressure. In the freeze-thawed sandstone with a "trunk-type" pore structure, the water in the trunk crack first freezes, and type I and type II freezing modes occur. That is, the unfrozen water in the secondary crack migrates to the trunk crack, and the unfrozen water in the secondary crack freezes in situ. During the freezing and thawing process of high-saturation rocks, the type I freezing mode mainly occurs, but the type II freezing mode causes secondary crack propagation, such that the adjacent cracks become connected, the pore connection parameters increase linearly, and the absolute permeability growth rate is the largest (Figure 12), which is consistent with the findings of Jia et al. [48]. However, the connectivity of low-saturation rocks remains basically unchanged after freeze-thaw cycles, which further indicates that saturation has a great influence on the freeze-thaw damage.

4.2. Influence of Prefabricated Fissures on the Freeze-Thaw Damage. Owing to the existence of prefabricated cracks, the ice segregation mechanism is more likely to occur. During rock freezing, the water in the pores around the

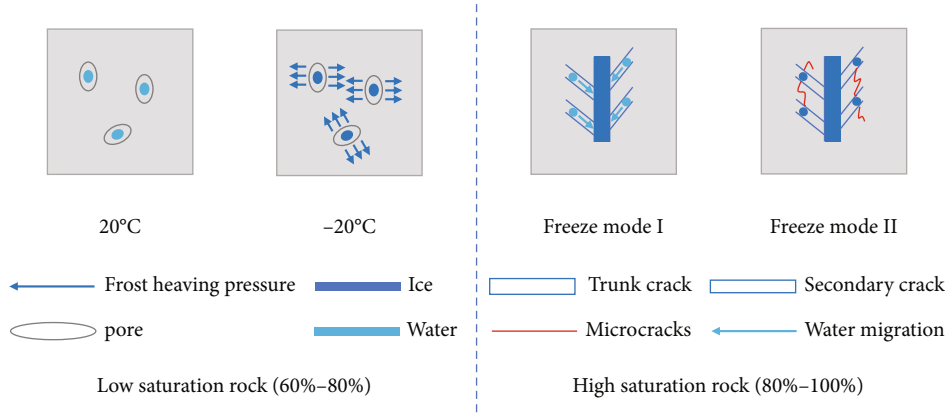

Figure 13: Mesoscopic freeze-thaw damage mechanism under the influence of different saturations.

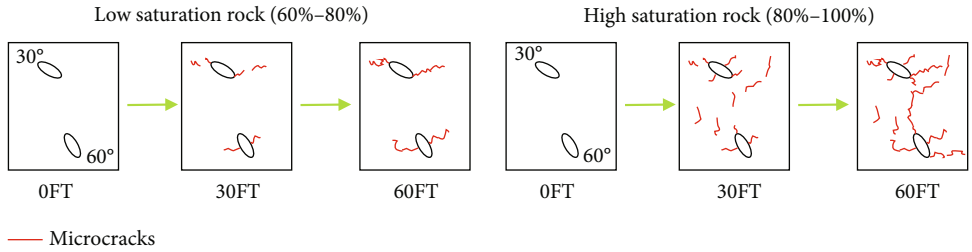

Figure 14: Damage evolution characteristics under the influence of prefabricated cracks.

prefabricated cracks freezes first, and the pore water further away from the prefabricated cracks has not yet frozen, which produces segregation potential; therefore, the water migrates to the pores around the prefabricated cracks. As a result, the microcracks in the rock bridge expand along the prefabricated cracks [49], and the damage evolution characteristics are shown in Figure 14.

For low saturation of the rock sample, the fracture extended laterally along the edge of the rock sample with the increase in the number of freeze-thaw cycles and at a prefabricated fracture inclination angle of 30°. For the prefabricated fracture inclination angle of 60°, the fracture first extended along the short axis of the ellipse. After 60 freeze-thaw cycles, microcracks also appeared around the prefabricated fracture inclination angle. Because of the high water content of the highly saturated rock samples, the double prefabricated cracks provided a channel for the seepage of the rock bridge during the freeze-thaw cycle. The main difference between high-saturation rock samples and low-saturation rock samples is that the rock bridge begins to be damaged. With the increase in the number of freeze-thaw cycles, the rock sample damage intensified. This is also evident from the analysis of the rock bridge in Section 3.3. The connectivity parameters demonstrated a linear change, which indicated that prefabricated cracks accelerated the seepage of water. The saturation is the main controlling factor in the freeze-thaw cycles of rock samples, which is similar to the findings of Al-Omari et al. [8].

In summary, the connection speed of microcracks for high-saturation rock samples is higher after freezing and thawing under the influence of prefabricated cracks, while the damage of low-saturation rock samples after freeze-thaw cycles under the influence of prefabricated cracks is small, and the freeze-thaw cycles have a limited influence on the freeze-thaw damage.

5. Conclusions

In this paper, the freeze-thaw damage of fractured sandstone at different saturation was studied based on CT technology and the three-dimensional fracture evolution characteristics of rock samples were analyzed. Based on the variation law of pores and throats and the connectivity parameters of the rock bridge, the freeze-thaw damage mechanism under the joint influence of the number of freeze-thaw cycles and prefabricated cracks was finally established. The critical saturation was determined to be 80% according to the variations of different parameters. The main conclusions are as follows:

(1) After completing the freeze-thaw cycles of rock samples with different saturations, the fractures demonstrated a similar development trend. For the 60° inclination angle of the ellipse, the fractures first expanded along the short axis of the ellipse. After the freeze-thaw cycles of low-saturation sandstone, the fracture area was found to be damaged, whereas the rock bridge had no sign of damage. The minimum fracture volume growth rate was only 29.9%. However, the fracture volume growth rate of fully saturated rock samples was 125% after 60 freeze-thaw cycles. The segregation potential generated by the ice separation mechanism will cause water to

migrate into the pores around the prefabricated fractures. Once the saturation exceeded 80%, the rock bridge started to damage and the degree of freeze-thaw damage was significantly greater than that of low-saturation sandstone

(2) The pore throat parameters, such as the number of pore throats, the maximum pore equivalent radius, the maximum throat equivalent radius, and the maximum throat length, can quantitatively characterize the damage changes of fractured sandstones with different saturations after freeze-thaw cycles. Due to the small frost-heaving pressure and no enough water to enter other pores, the low-saturation sandstone mainly causes the throat radius between pores to expand and generate more pores around the pores after freeze-thaw cycles. After the freeze-thaw cycling, the high-saturation sandstone is under the action of higher frost-heaving pressure and pore water pressure, which mainly leads to the connection of macropores at larger distances to form microcracks

(3) The pore size distribution can reflect the complex pore structure and can accurately describe the mesoscopic structure changes in sandstone. The pores can be divided according to their size: small pores, mesopores, and macropores. Sandstones with different saturations exhibit different changes for the different types of pores during the freeze-thaw process. In the initial state, the proportion of mesopores is 70%–80%, and when the saturation is greater than 80%, due to the hydrostatic pressure mainly leads to the formation of microcracks, the freeze-thaw damage mainly shows that the proportion of small pores decreases and the increment of the proportion of mesopores is the largest

(4) The coordination number, tortuosity, and absolute permeability can characterize the connectivity of pores under freeze-thaw action. The results show that the coordination number of first decreases and then increases with increases in the freeze-thaw times, and the tortuosity first increases and then decreases; the absolute permeability increases linearly. The pore coordination number and absolute permeability of fractured rocks with high saturation increase linearly with increases in the freeze-thaw times, while the tortuosity decreases linearly. The freeze-thaw damage is mainly caused by the migration of unfrozen water to the trunk crack and the unfrozen water in the secondary crack freezes in situ

Data Availability

The data used to support the study is available within the article.

Conflicts of Interest

The authors declare that they have no conflict of interest.

Acknowledgments

This research was supported by the National Natural Science Foundation of China (42277182, 11972283) and Natural Science Foundation of Shaanxi Province (2017JM1039).

References

[1] M. Deprez, T. De Kock, G. De Schutter, and V. Cnudde, "A review on freeze-thaw action and weathering of rocks," *Earth-Science Reviews*, vol. 203, article 103143, 2020.

[2] T. Y. Liu, C. Y. Zhang, P. Cao, and K. P. Zhou, "Freeze-thaw damage evolution of fractured rock mass using nuclear magnetic resonance technology," *Cold Regions Science and Technology*, vol. 170, article 102951, 2020.

[3] A. Momeni, Y. Abdilor, G. R. Khanlari, M. Heidari, and A. A. Sepahi, "The effect of freeze–thaw cycles on physical and mechanical properties of granitoid hard rocks," *Bulletin of Engineering Geology and the Environment*, vol. 75, no. 4, pp. 1649–1656, 2020.

[4] S. B. Huang, Q. S. Liu, A. P. Cheng, and Y. Z. Liu, "A statistical damage constitutive model under freeze-thaw and loading for rock and its engineering application," *Cold Regions Science and Technology*, vol. 145, pp. 142–150, 2018.

[5] Y. Ye, L. Li, and X. J. Xu, "Physical and mechanical properties of transmission line galloping under the action of freezing and thawing in variable temperature range," *Advances in Civil Engineering*, vol. 2021, Article ID 8368289, 10 pages, 2021.

[6] Y. J. Ma, *Experimental Study on Deterioration Mechanism of Cretaceous during the Construction of Mine Shafts in Western Area of China*, China University of Mining and Technology, Beijing, 2019, Doctoral thesis.

[7] Y. Z. Liu, Y. T. Cai, S. B. Huang, Y. L. Guo, and G. F. Liu, "Effect of water saturation on uniaxial compressive strength and damage degree of clay-bearing sandstone under freeze-thaw," *Bulletin of Engineering Geology and the Environment*, vol. 79, no. 4, pp. 2021–2036, 2020.

[8] A. Al-Omari, K. Beck, X. Brunetaud, Á. Török, and M. Al-Mukhtar, "Critical degree of saturation: a control factor of freeze-thaw damage of porous limestones at Castle of Chambord, France," *Engineering Geology*, vol. 185, pp. 71–80, 2015.

[9] S. B. Huang, Y. T. Cai, Y. Z. Liu, and G. F. Liu, "Experimental and theoretical study on frost deformation and damage of red sandstones with different water contents," *Rock Mechanics and Rock Engineering*, vol. 54, no. 8, pp. 4163–4181, 2021.

[10] S. B. Huang, Y. B. He, S. L. Yu, and C. Cai, "Experimental investigation and prediction model for UCS loss of unsaturated sandstones under freeze-thaw action," *International Journal of Mining Science and Technology*, vol. 32, no. 1, pp. 41–49, 2022.

[11] Z. L. Zhou, X. Cai, D. Ma et al., "Water saturation effects on dynamic fracture behavior of sandstone," *International Journal of Rock Mechanics and Mining Sciences*, vol. 114, pp. 46–61, 2019.

[12] T. C. Chen, M. R. Yeung, and N. Mori, "Effect of water saturation on deterioration of welded tuff due to freeze-thaw action," *Cold Regions Science and Technology*, vol. 38, no. 2-3, pp. 127–136, 2004.

[13] D. Guha Roy, T. N. Singh, J. Kodikara, and R. Das, "Effect of water saturation on the fracture and mechanical properties of sedimentary rocks," *Rock Mechanics and Rock Engineering*, vol. 50, no. 10, pp. 2585–2600, 2017.

[14] W. J. Xiao, D. M. Zhang, X. J. Wang, H. Yang, X. Wang, and C. Wang, "Research on microscopic fracture morphology and damage constitutive model of red sandstone under seepage pressure," *Natural Resources Research*, vol. 29, no. 5, pp. 3335–3350, 2020.

[15] A. Keneti and B. A. Sainsbury, "Characterization of strain-burst rock fragments under a scanning electron microscope - an illustrative study," *Engineering Geology*, vol. 246, pp. 12–18, 2018.

[16] L. Qin, C. Zhai, S. M. Liu, J. Xu, G. Yu, and Y. Sun, "Changes in the petrophysical properties of coal subjected to liquid nitrogen freeze-thaw - a nuclear magnetic resonance investigation," *Fuel*, vol. 194, pp. 102–114, 2017.

[17] X. P. Zhou, C. Q. Li, and L. S. Zhou, "The effect of microstructural evolution on the permeability of sandstone under freeze-thaw cycles," *Cold Regions Science and Technology*, vol. 177, article 103119, 2020.

[18] N. Thiemeyer, J. Habersetzer, M. Peinl, G. Zulauf, and J. Hamme, "The application of high resolution x-ray computed tomography on naturally deformed rock salt: multi-scale investigations of the structural inventory," *Journal of Structural Geology*, vol. 77, pp. 92–106, 2015.

[19] C. B. Jiang, X. D. Liu, W. S. Wang, W. H. Wei, and M. K. Duan, "Three-dimensional visualization of the evolution of pores and fractures in reservoir rocks under triaxial stress," *Powder Technology*, vol. 378, pp. 585–592, 2021.

[20] J. Park, C. U. Hyun, and H. D. Park, "Changes in microstructure and physical properties of rocks caused by artificial freeze–thaw action," *Bulletin of Engineering Geology and the Environment*, vol. 74, no. 2, pp. 555–565, 2015.

[21] M. Deprez, T. De Kock, G. De Schutter, and V. Cnudde, "The role of ink-bottle pores in freeze-thaw damage of oolithic limestone," *Construction and Building Materials*, vol. 246, article 118515, 2020.

[22] Y. Shields, E. Garboczi, J. Weiss, and Y. Farnam, "Freeze-thaw crack determination in cementitious materials using 3D X-ray computed tomography and acoustic emission," *Cement and Concrete Composites*, vol. 89, pp. 120–129, 2018.

[23] Y. J. Song, H. Tan, H. M. Yang, S. Chen, Y. Che, and J. Chen, "Fracture evolution and failure characteristics of sandstone under freeze-thaw cycling by computed tomography," *Engineering Geology*, vol. 294, article 106370, 2021.

[24] J. Q. Mu, X. J. Pei, R. Q. Huang, N. Rengers, and X. Q. Zou, "Degradation characteristics of shear strength of joints in three rock types due to cyclic freezing and thawing," *Cold Regions Science and Technology*, vol. 138, pp. 91–97, 2017.

[25] H. L. Fu, J. B. Zhang, Z. Huang, Y. Shi, and W. Chen, "A statistical model for predicting the triaxial compressive strength of transversely isotropic rocks subjected to freeze-thaw cycling," *Cold Regions Science and Technology*, vol. 145, pp. 237–248, 2018.

[26] S. B. Huang, Q. S. Liu, Y. Z. Liu, Y. Kang, A. Cheng, and Z. Ye, "Frost heaving and frost cracking of elliptical cavities (fractures) in low- permeability rock," *Engineering Geology*, vol. 234, pp. 1–10, 2018.

[27] S. B. Huang, Y. Z. Liu, Y. L. Guo, Z. L. Zhang, and Y. T. Cai, "Strength and failure characteristics of rock-like material containing single crack under freeze-thaw and uniaxial compression," *Cold Regions Science and Technology*, vol. 162, pp. 1–10, 2019.

[28] J. J. Tian, D. J. Xu, and T. H. Liu, "An experimental investigation of the fracturing behaviour of rock-like materials containing two V-shaped parallelogram flaws," *International Journal of Mining Science and Technology*, vol. 30, no. 6, pp. 777–783, 2020.

[29] J. X. Ren, "Real time CT testing on damage evolution characteristics of frozen cracked-sandstone under uniaxial compression," *Chinese Journal of Rock Mechanics and Engineering*, vol. 24, no. 1, pp. 74–77, 2005.

[30] Y. Bai, R. L. Shan, Y. Ju et al., "Experimental study on the strength, deformation and crack evolution behaviour of red sandstone samples containing two ice-filled fissures under triaxial compression," *Cold Regions Science and Technology*, vol. 174, article 103061, 2020.

[31] N. Gallagher and G. Wise, "A theoretical analysis of the properties of median filters," *IEEE Transactions on Acoustics, Speech, and Signal Processing*, vol. 29, no. 6, pp. 1136–1141, 1981.

[32] S. Q. Yang, Y. H. Huang, W. L. Tian, and J. B. Zhu, "An experimental investigation on strength, deformation and crack evolution behavior of sandstone containing two oval flaws under uniaxial compression," *Engineering Geology*, vol. 217, pp. 35–48, 2017.

[33] X. Chen, Z. H. Liao, and D. J. Li, "Experimental study of effects of joint inclination angle and connectivity rate on strength and deformation properties of rock masses under uniaxial compression," *Chinese Journal of Rock Mechanics and Engineering*, vol. 30, no. 4, pp. 781–789, 2011.

[34] Y. X. Che, Y. J. Song, J. X. Ren et al., "Creep characteristics of different saturated states of red sandstone after freeze-thaw cycles," *Geofluids*, vol. 2021, Article ID 6622380, 13 pages, 2021.

[35] R. D. Peng, Y. C. Yang, Y. Ju, L. T. Mao, and Y. M. Yang, "Computation of fractal dimension of rock pores based on gray CT images," *Chinese Science Bulletin*, vol. 56, no. 31, pp. 3346–3357, 2011.

[36] P. C. Baveye, M. Laba, W. Otten et al., "Observer-dependent variability of the thresholding step in the quantitative analysis of soil images and X-ray microtomography data," *Geoderma*, vol. 157, no. 1-2, pp. 51–63, 2010.

[37] A. N. Houston, S. Schmidt, A. M. Tarquis, W. Otten, P. C. Baveye, and S. M. Hapca, "Effect of scanning and image reconstruction settings in X-ray computed microtomography on quality and segmentation of 3D soil images," *Geoderma*, vol. 207, pp. 154–165, 2013.

[38] W. B. Lindquist, S. M. Lee, D. A. Coker, K. W. Jones, and P. Spanne, "Medial axis analysis of void structure in three-dimensional tomographic images of porous media," *Journal of Geophysical Research: Solid Earth*, vol. 101, no. B4, pp. 8297–8310, 1996.

[39] A. M. S. Lala, "A novel model for reservoir rock tortuosity estimation," *Journal of Petroleum Science and Engineering*, vol. 192, article 107321, 2020.

[40] Z. Bassiouni, *"Theory, Measurement, and Interpretation of Well Logs", Dallas, TX, USA: Henry L*, Society of Petroleum Engineers, Doherty Memorial Fund of AIME, 1994.

[41] M. Matyka, A. Khalili, and Z. Koza, "Tortuosity-porosity relation in porous media flow," *Physical Review E*, vol. 78, no. 2, article 026306, 2008.

[42] J. H. Lu, Z. L. Guo, Z. H. Chai, and B. C. Shi, "Numerical study on the tortuosity of porous media via lattice Boltzmann method," *Communications in Computational Physics*, vol. 6, no. 2, p. 354, 2009.

[43] X. W. Tang, Z. F. Sun, and G. C. Cheng, "Simulation of the relationship between porosity and tortuosity in porous media with cubic particles," *Chinese Physics B*, vol. 21, no. 10, article 100201, 2012.

[44] H. Darcy, *Les Fontaines Publiques de la Ville de Dijon: Exposition et Application*, Victor Dalmont, Paris, 1856.

[45] O. Coussy and P. Monteiro, "Unsaturated poroelasticity for crystallization in pores," *Computers and Geotechnics*, vol. 34, no. 4, pp. 279–290, 2007.

[46] H. L. Jia, F. Zi, G. S. Yang et al., "Influence of pore water (ice) content on the strength and deformability of frozen argillaceous siltstone," *Rock Mechanics and Rock Engineering*, vol. 53, no. 2, pp. 967–974, 2020.

[47] J. Ruedrich, D. Kirchner, and S. Siegesmund, "Physical weathering of building stones induced by freeze–thaw action: a laboratory long-term study," *Environmental Earth Sciences*, vol. 63, no. 7-8, pp. 1573–1586, 2011.

[48] H. L. Jia, S. Ding, F. Zi, Y. H. Dong, and Y. J. Shen, "Evolution in sandstone pore structures with freeze-thaw cycling and interpretation of damage mechanisms in saturated porous rocks," *Catena*, vol. 195, article 104915, 2020.

[49] H. L. Jia, W. Xiang, and M. Krautblatter, "Quantifying rock fatigue and decreasing compressive and tensile strength after repeated freeze-thaw cycles," *Permafrost and Periglacial Processes*, vol. 26, no. 4, pp. 368–377, 2015.